Stability of Zircon and Its Isotopic Ratios in High-Temperature Fluids: Long-Term (4 months) Isotope Exchange Experiment at 850°C and 50 MPa

Ilya N. Bindeman[1,2]*, Axel K. Schmitt[3], Craig C. Lundstrom[4] and Richard L. Hervig[5]

[1] Earth Sciences, University of Oregon, Eugene, OR, United States, [2] Fersman Mineralogical Museum, Moscow, Russia, [3] Institute of Earth Sciences, Heidelberg University, Heidelberg, Germany, [4] Department of Geology, University of Illinois at Urbana-Champaign, Champaign, IL, United States, [5] School of Earth and Space Exploration, Arizona State University, Tempe, AZ, United States

Stability of zircon in hydrothermal fluids and vanishingly slow rates of diffusion identify zircon as a reliable recorder of its formation conditions in recent and ancient rocks. Debate, however, persists on how rapidly oxygen and key trace elements (e.g., Li, B, Pb) diffuse when zircon is exposed to silicate melt or hot aqueous fluids. Here, we report results of a nano- to micrometer-scale investigation of isotopic exchange using natural zircon from Mesa Falls Tuff (Yellowstone) treated with quartz-saturated, isotopically (^{18}O, D, ^{7}Li, and ^{11}B) labeled water with a nominal $\delta^{18}O$ value of +450‰ over 4 months at 850°C and 50 MPa. Frontside (crystal rim inwards) $\delta^{18}O$ depth profiling of zircon by magnetic sector SIMS shows initially high but decreasing $^{18}O/^{16}O$ over a ~130 nm non-Fickian profile, with a decay length comparable to the signal from surficial Au coating deposited onto zircon. In contrast, backside (crystal interior outwards) depth profiling on a 2-3 μm thick wafer cut and thinned from treated zircon by focused ion beam (FIB) milling lacks any significant increase in $^{18}O/^{16}O$ during penetration of the original surface layer. Near-surface time-of-flight (TOF-SIMS) frontside profiles of uncoated zircon from 4-month and 1-day-long experiments as well as untreated zircons display similar enrichments of ^{18}O over a distance of ~20 nm. All frontside ^{18}O profiles are here interpreted as transient surface signals from nm-thick surface enrichment or contamination unrelated to diffusion. Likewise, frontside depth profiling of H, Li, and B isotopes are similar for long- and short-duration experiments. Additionally, surface U-Pb dating of zircon from the 4-month experiment returned U-Pb ages by depth profiling with ~1 μm penetration that were identical to untreated samples. Frontside and backside depth-profiling thus demonstrate that diffusive ^{18}O enrichment in the presence of H_2O is much slower than predicted from experiments in Watson and Cherniak (1997). Instead, intracrystalline exchange of oxygen between fluid and zircon in wet experimental conditions with excess silica occurred over length-scales equivalent to those predicted for dry diffusion. Oxygen diffusion coefficients

even under wet conditions and elevated temperatures (850°C) are $\leq$1–3 $\times$ 10^{-23} m^2/s, underscoring a virtual lack of oxygen diffusion and an outstanding survivability of zircons and its isotopic inventory under most metamorphic and hydrothermal conditions.

INTRODUCTION

Zircon is a refractory mineral used in many geochronological and petrochronological applications involving igneous, metamorphic, and sedimentary rocks (Hanchar and Hoskin, 2003; Schaltegger et al., 2015; Rubatto, 2017; Schaltegger and Davies, 2017). Zircon in particular is the only reliably identifiable material from the Hadean Earth and thus of prime importance for gleaning insights into processes within the first few 100 Ma after planet formation (e.g., Trail et al., 2007; Harrison, 2009; Valley et al., 2015). Steady improvements in microanalytical techniques over the past decades have resulted in an increased ability to analyze and interpret variations of ages, trace elements, and isotopic compositions at increasingly finer spatial resolution, lately including Atom Probe Tomography (APT) with mono-atomic resolution (Valley et al., 2015). Models of kinetics of zircon growth predict μm-scale variations, recording varying P-T-X_{H2O} conditions over months to years of zircon growth (Melnik and Bindeman, 2018). It is thus important to understand to what extent these variations, which are now available to be resolved by nm-scale microanalytical methods, record primary growth features vs. subsequent diffusion. Oxygen isotopic studies of zircon are of particular importance for deducing the role of surface waters as well as magmatic and metamorphic fluids during zircon crystallization and its subsequent history. Key aims of such studies have been to (1) establish zircon stability and solubility in hot silica-saturated hydrothermal solutions, such as those found in large silicic calderas worldwide and possibly also on large impact craters on Earth and Mars (e.g., Abramov and Kring, 2005; Abramov et al., 2013; Bindeman and Simakin, 2014); (2) derive metamorphic and magmatic heating timescales from intra-crystal oxygen isotopic gradients, or likewise other elements (e.g., Bowman et al., 2011; Claesson et al., 2016; Roberts et al., 2018); (3) assess the significance of U-Pb ages and oxygen isotopic signatures of Hadean zircons with protracted and poorly constrained polymetamorphic histories (e.g., Wilde et al., 2001; Cavosie et al., 2006; Harrison et al., 2008); and (4) provide criteria to identify "hydrothermal" zircon and use it as a tool to date post-magmatic or tectonic fluid-rock interaction (e.g., Hanchar and Hoskin, 2003; Schaltegger, 2007). To fully interpret the zircon and other accessory mineral record in the context of these diverse research directions, it is essential to better constrain how zircon responds to hot fluid environments, and if and how fast essential components such as oxygen are mobilized under these conditions.

Watson and Cherniak (1997) have performed pioneering studies of oxygen diffusion in zircon, mostly through using the nuclear attenuation t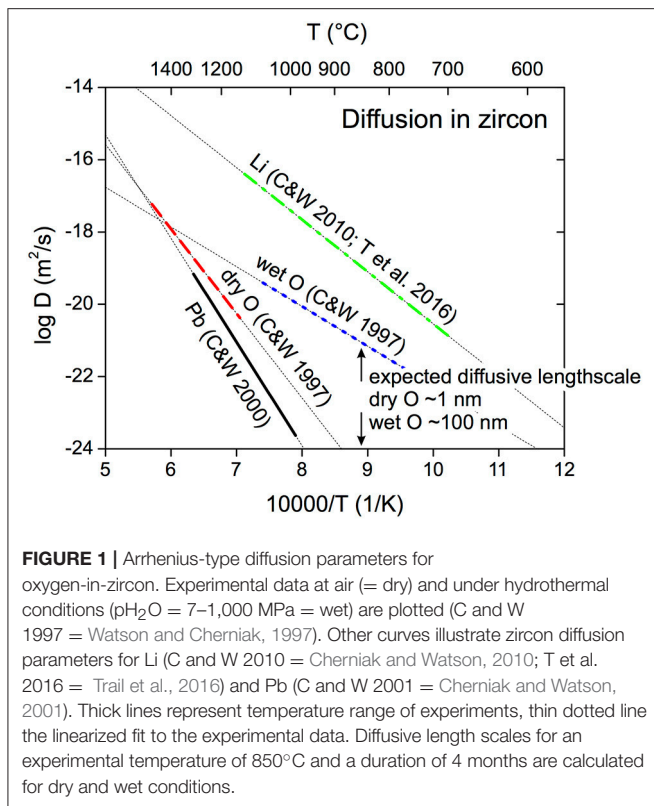echnique of Rutherford Backscatter Spectroscopy (RBS) but also using surface analysis by small magnet radius SIMS instruments. They obtained Arrhenius diffusion relationships (**Figure 1**) for both wet and dry conditions, whereby "wet" is short-hand for diffusion in the presence of water at pH_2O >7 MPa. Thus the majority of diffusion in nature should proceed according to this water-present mechanism. Their results suggest that $\delta^{18}O$ in zircon with grain diameters of 100 μm should completely exchange with fluid at T >750°C within 10^4 year time-scales. In the absence of H_2O, zircon held at T <800°C for 10^6 years would experience diffusive exchange over much smaller (<2 μm) distances with its isotopic composition essentially unchanged in the crystal interior. Some natural studies advocate for a reset of $\delta^{18}O$ in metamorphic environments (Claesson et al., 2016; Roberts et al., 2018).

Our studies of natural metamorphic zircons from Karelia (**Figure 2**) with the largest yet-measured core-rim difference in $\delta^{18}O$ of 23‰ demonstrate that zoning was preserved over length-scales much smaller than predicted for wet diffusion prevalent under most geologic conditions. The rocks in question have experienced high-temperature (>750°C) amphibolite- to granulite-grade metamorphism over durations of >10^8 years (Bindeman et al., 2014). Similar observations supporting preservation of metamorphic rims were made by Page et al. (2007) and Peck et al. (2003). Here we re-visit diffusivities in zircon by performing a long-term zircon exchange/diffusion experiment lasting 4 months at 850°C and high water pressure (pH_2O = P_{total} = 50 MPa). In this longest yet-reported experiment for zircon, we take advantage of the analytical improvements over the past 20 years since the study of Watson and Cherniak (1997). Although our main goal is to constrain oxygen diffusion parameters in zircon, we opportunistically used the same experiment to assess mobilization and transport of H, Li, B, and Pb in zircon.

MATERIALS AND METHODS
Experimental and Analytical Goals

The slow diffusion of oxygen and other elements in zircon even at high temperature and in the presence of H_2O (Watson and Cherniak, 1997) requires long-term experiments to generate diffusion over length-scales amenable to depth profiling by SIMS (**Figure 3**). To use depth profiling in frontside and backside modes (**Figure 3**), we targeted prism faces of natural zircon rather than sectioned zircon where surface damage caused by sawing and polishing could lead to spurious diffusion behavior (e.g., Reed and Wuensch, 1980). Expected profiles for

FIGURE 1 | Arrhenius-type diffusion parameters for oxygen-in-zircon. Experimental data at air (= dry) and under hydrothermal conditions (pH_2O = 7–1,000 MPa = wet) are plotted (C and W 1997 = Watson and Cherniak, 1997). Other curves illustrate zircon diffusion parameters for Li (C and W 2010 = Cherniak and Watson, 2010; T et al. 2016 = Trail et al., 2016) and Pb (C and W 2001 = Cherniak and Watson, 2001). Thick lines represent temperature range of experiments, thin dotted line the linearized fit to the experimental data. Diffusive length scales for an experimental temperature of 850°C and a duration of 4 months are calculated for dry and wet conditions.

FIGURE 2 | Secondary ionization mass spectrometry (SIMS) oxygen isotope analyses for a high-grade metamorphic zircon from Karelia. Data were generated on the UCLA CAMECA ims 1270 using a pre-cesiated surface and a ~1 μm Ga+ focused ion beam. A large isotopic contrast between the rim and the core was also detected with two individual spot analyses using a ~15 μm Cs+ beam where precision was ±0.25‰ compared to ±4‰ for the Ga+ analyses. The Ga+ profile indicates isotopic equilibration over a length scale <5 μm. Preservation of such a steep isotopic profile attests virtual lack of oxygen diffusion happening over millions of years at T<700–750°C (Bindeman et al., 2014).

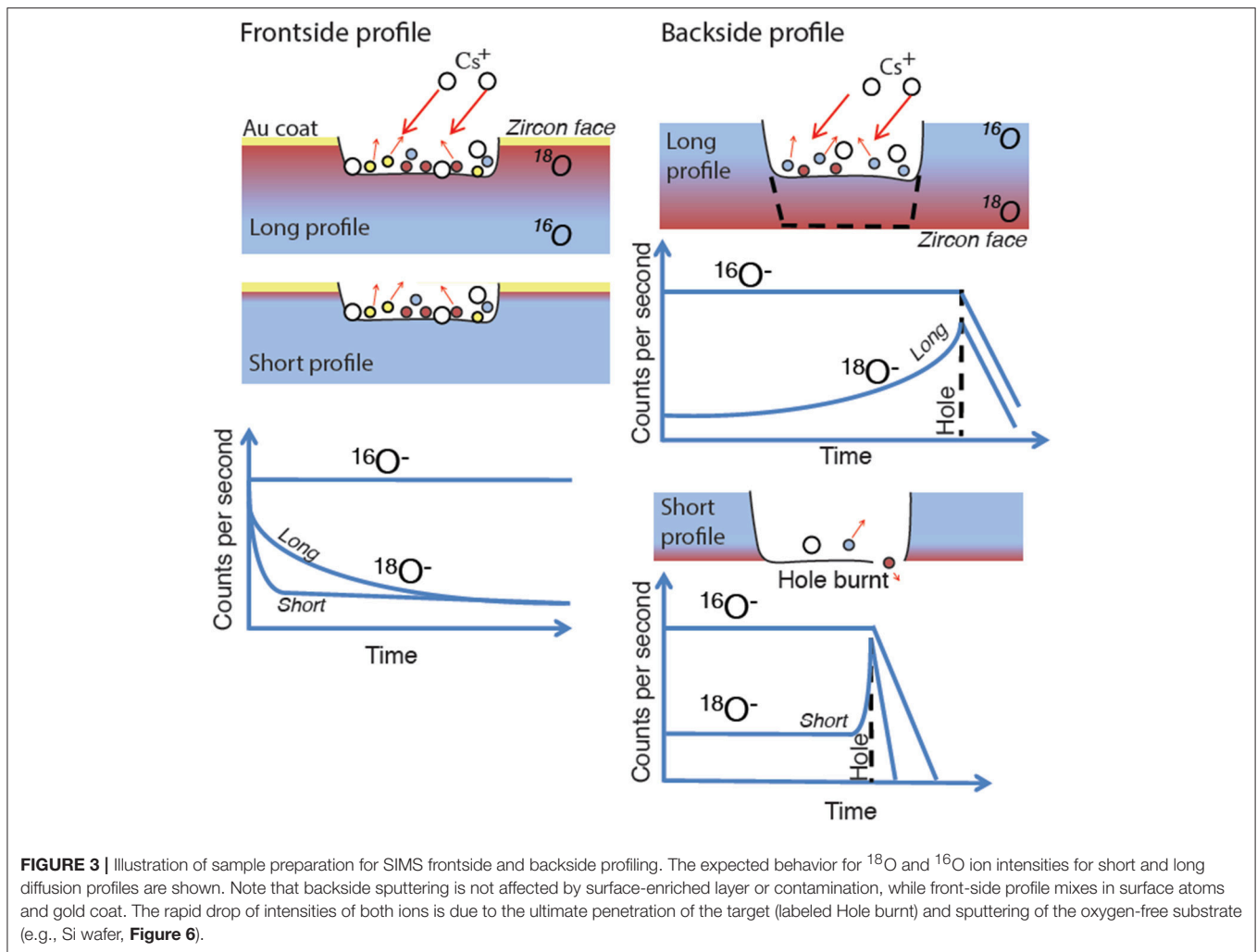frontside and backside profiles are schematically illustrated in **Figure 4**.

Starting Materials

Starting materials included natural zircon, rutile and quartz with previously measured distinct and homogeneous $\delta^{18}O$ compositions. Zircon crystals (sample MFT-1; Bindeman et al., 2008) from the Mesa Falls tuff of Yellowstone, Wyoming, USA, were chosen for their large size (150–300 μm in long dimension, 80–150 μm in short), homogeneous age and uniform oxygen isotope rim (20–40 μm) compositions of $\delta^{18}O$ = 3.6 ± 0.3‰ (all values given as V-SMOW at ±2σ uncertainties; Bindeman et al., 2008; Wotzlaw et al., 2015) as determined by SIMS using two different ion microprobes. Zircon from Mesa Falls tuff also has yielded indistinguishable isotope dilution thermal ionization mass spectrometry (CA-ID-TIMS) ages of 1.31 Ma in two separate studies of Wotzlaw et al. (2015) and Rivera et al. (2016). Rutile crystals ($\delta^{18}O$ values of −29‰, sample K1; Bindeman et al., 2014) of the 1.87 Ga Belomorian metamorphic belt in Karelia, Russia, were added to the experimental charge in an attempt to investigate oxygen diffusion in rutile; however some rutile surfaces developed dissolution etching (**Figure 4B**) and thus rutile was not considered further. Quartz crystals from Bishop Tuff ($\delta^{18}O$ = +8.24‰, sample LV748, Bindeman and Valley 2002) Long Valley caldera, California, USA) were included in the starting material as single crystals (**Figure 5c**) and fragments. They developed variable amounts of dissolution and reprecipitation during the experiment (**Figures 4C–E**).
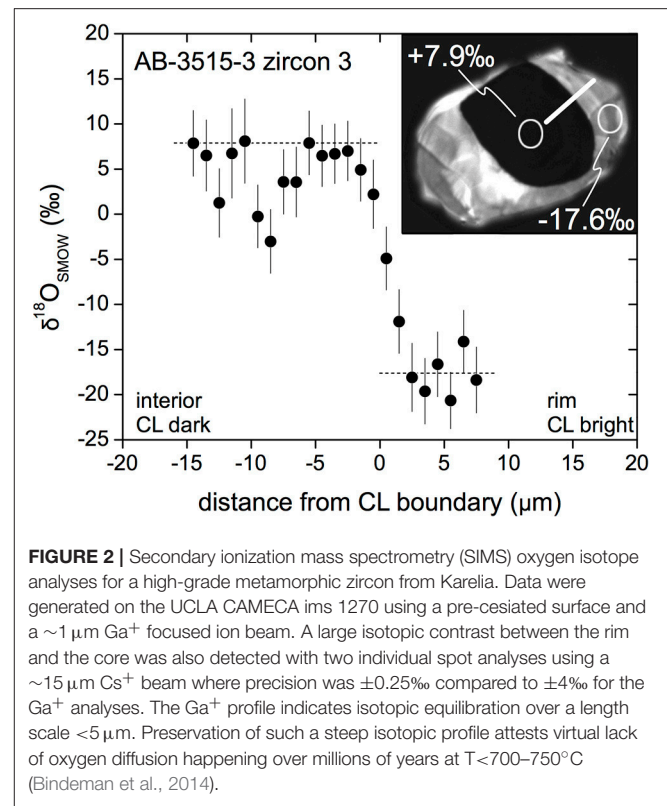
Zircon, rutile and quartz crystals were immersed in $\delta^{18}O$ and δD enriched water with $\delta^{18}O$ = +450‰ and δD = +350 ‰), which was obtained by mixing of Cambridge Isotope Laboratories, Inc. 10% ^{18}O water (lot OLM-240-10-0) with in-house labeled water (+56‰ $\delta^{18}O$, +650‰ δD). Furthermore, milligram quantities of isotopically enriched (nearly pure ^7Li and ^{11}B from Ceradyne Corporation) were added as single drops of dissolved B(OH)$_3$ and Li(OH). Minerals and water were sealed in a single gold capsule in the following quantities: 6.4 mg of minerals (quartz, zircon, rutile in weight proportions 1:3:2) and 76 mg of doped water solution. At these proportions, minor isotopes are present in significant excess compared to their natural abundances in the crystals.

Experimental Design and Conditions

The choice of experimental duration (~4 months) and temperature (~850°C) for the experiment were selected based on the "wet" diffusion coefficients from Watson and Cherniak (1997), which predict an oxygen isotopic diffusive penetration over ~93 nm in zircon, whereas diffusive length scales for "dry" diffusion coefficients are only ~1 nm. Experiment ZE1 was performed in a cold seal pressure vessel for ~4 months between 6/13/2011 at 14:00 h and 10/12/11 at 16:00 h at the University of Illinois. Temperature control via thermocouple indicated constant T at 850 ± 1°C, and pressure was maintained at 48 MPa for most of the time until it started to drop rapidly to 45 MPa on 10/12/11. The experiment was then quenched to prevent capsule rupture after a total run time of 1.04616 × 10^7 s.

FIGURE 3 | Illustration of sample preparation for SIMS frontside and backside profiling. The expected behavior for ^{18}O and ^{16}O ion intensities for short and long diffusion profiles are shown. Note that backside sputtering is not affected by surface-enriched layer or contamination, while front-side profile mixes in surface atoms and gold coat. The rapid drop of intensities of both ions is due to the ultimate penetration of the target (labeled Hole burnt) and sputtering of the oxygen-free substrate (e.g., Si wafer, **Figure 6**).

The sealed capsule weighed exactly 632.90 mg before and after the experiment, indicating no leakage of water or preferential hydrogen loss for this long-duration run.

The same batch of starting materials was also used for a brief ("zero-time") experiment ZE2, where the capsule was pressurized and heated under identical conditions as for ZE1. This run, however, was terminated and the experimental charge quenched after 24 h. Capsule ZE2 weighed the same before and after the experiment (547.50 mg) and upon opening registered an audible hiss, indicating that no leakage occurred. Experimental products were extracted and examined optically, by scanning electron microscopy (SEM), electron microprobe, and multiple ion beam instruments (see below).
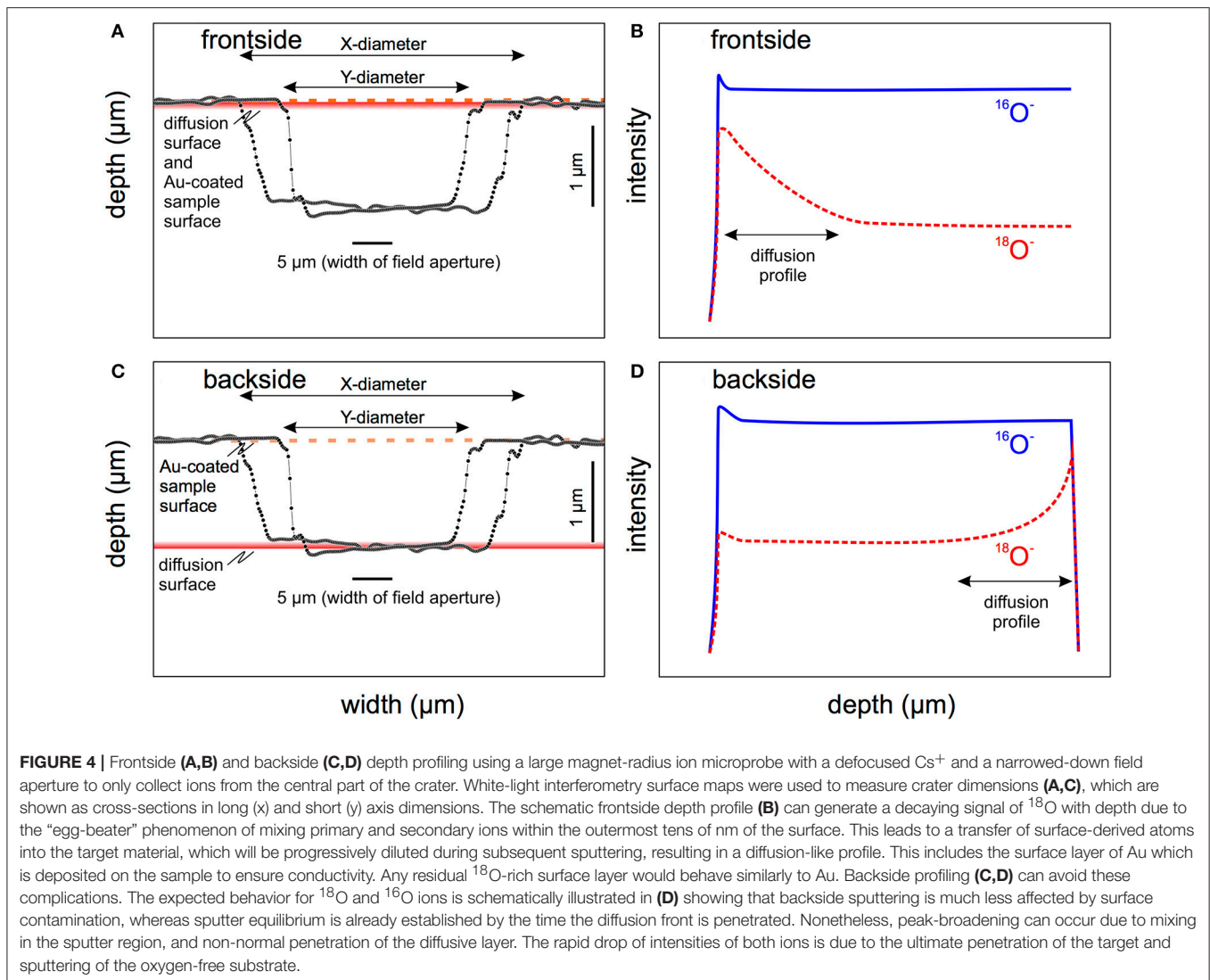
Reaction Products

ZE1 zircon crystals remained intact except for negative crystal shape molds of apatite crystals formerly attached to the zircon surface (**Figures 5a,f**). These imprints retained sharp-angle morphology, suggesting negligible zircon dissolution and re-precipitation. By contrast, a visually estimated ~50% of the original quartz crystals became dissolved and re-precipitated as

amorphous or microcrystalline quartz on capsule surfaces and other minerals (**Figures 5c,d**). Rutile experienced reprecipitation and surface etching (**Figures 5b,e**). The exception is one rutile crystal, which was covered with μm-sized aggregates tentatively identified by electron microprobe as titanite. The calcium required for titanite formation was likely derived from the dissolution of apatite present at crystal surfaces. Reaction products of 1-day long ZE2 experiment remained visibly unchanged, with the exception of etching of quartz surfaces.

Estimates of Solubilities and the Effects of Solution-Reprecipitation

For our experimental conditions, thermodynamic data from Shock et al. (1989) would predict 350 ppm SiO_2 concentration in hydrothermal fluids. Using experimental data from Fournier (1985) on quartz solubility, the saturation concentration is 1.7 mg/g SiO_2; thus only ~13% of the ~1 mg of quartz added to the experiment would become dissolved. However, a significant amount of the original quartz crystals were obliterated by the end of the experiment, and replaced by finely crystalline SiO_2

**FIGURE 4 |** Frontside **(A,B)** and backside **(C,D)** depth profiling using a large magnet-radius ion microprobe with a defocused Cs$^+$ and a narrowed-down field aperture to only collect ions from the central part of the crater. White-light interferometry surface maps were used to measure crater dimensions **(A,C)**, which are shown as cross-sections in long (x) and short (y) axis dimensions. The schematic frontside depth profile **(B)** can generate a decaying signal of ^{18}O with depth due to the "egg-beater" phenomenon of mixing primary and secondary ions within the outermost tens of nm of the surface. This leads to a transfer of surface-derived atoms into the target material, which will be progressively diluted during subsequent sputtering, resulting in a diffusion-like profile. This includes the surface layer of Au which is deposited on the sample to ensure conductivity. Any residual ^{18}O-rich surface layer would behave similarly to Au. Backside profiling **(C,D)** can avoid these complications. The expected behavior for ^{18}O and ^{16}O ions is schematically illustrated in **(D)** showing that backside sputtering is much less affected by surface contamination, whereas sputter equilibrium is already established by the time the diffusion front is penetrated. Nonetheless, peak-broadening can occur due to mixing in the sputter region, and non-normal penetration of the diffusive layer. The rapid drop of intensities of both ions is due to the ultimate penetration of the target and sputtering of the oxygen-free substrate.

aggregates, suggesting that most quartz experienced solution-repreciptation (**Figure 5d**), with only some large quartz crystals remaining intact. This is consistent with the fluid phase remaining silica saturated over the entire duration of the experiment, thus assuring zircon stability. If the fluid were silica-undersaturated, zircon would have broken down to baddeleyite or possibly vlasovite ($Na_2ZrSi_4O_{11}$) (e.g., Ayers et al., 2012), whereby Na would have been mobilized from melt, apatite, or feldspar inclusions within Bishop quartz. Baddeleyite is also common in silica undersaturated, mafic and ultramafic rocks. Zircon solubility in silica-saturated aqueous solutions ($a_{SiO2} = 1$) was determined by Ayers and Watson (1991), Ayers et al. (2012), and Bernini et al. (2013). At our experimental conditions, predicted solubility is ∼0.034 ppm Zr/g fluid using the Bernini et al. (2013) solubility parameterization; this translates to a loss of about 23 ng of zircon to 76 mg of saturated solution, or 0.0008% of the loaded zircon. The total surface area of ∼50 loaded 200 × 100 μm zircons is ∼5 mm^2, which means that dissolution of a sub-monoatomic layer 0.01 nm in thickness would be sufficient

to saturate the solution. However, we anticipate that zircon preferentially was dissolved on tips and ridges, with little effect on the interiors of zircon prism surfaces. Rutile solubility is ∼100 times higher than for zircon under the same P-T conditions and a saturated solution contains ∼3 μg/g dissolved TiO$_2$ (Ayers and Watson, 1993; Audětat and Keppler, 2005; Manning et al., 2008) explaining why it developed etching on some surfaces (**Figure 5**).

ANALYTICAL INVESTIGATION: SURFACE ANALYSIS BY DEPTH PROFILING

Overview

Zircon crystals from experimental run products (**Figure 5**) measuring at least 100 μm in width and 300–500 μm in length were hand-picked and cleaned by rubbing with cotton-swabs under a microscope, then ultrasonically cleaned in distilled 18 MΩ water three times for 15 min to remove surface contamination; after this procedure, most crystals looked
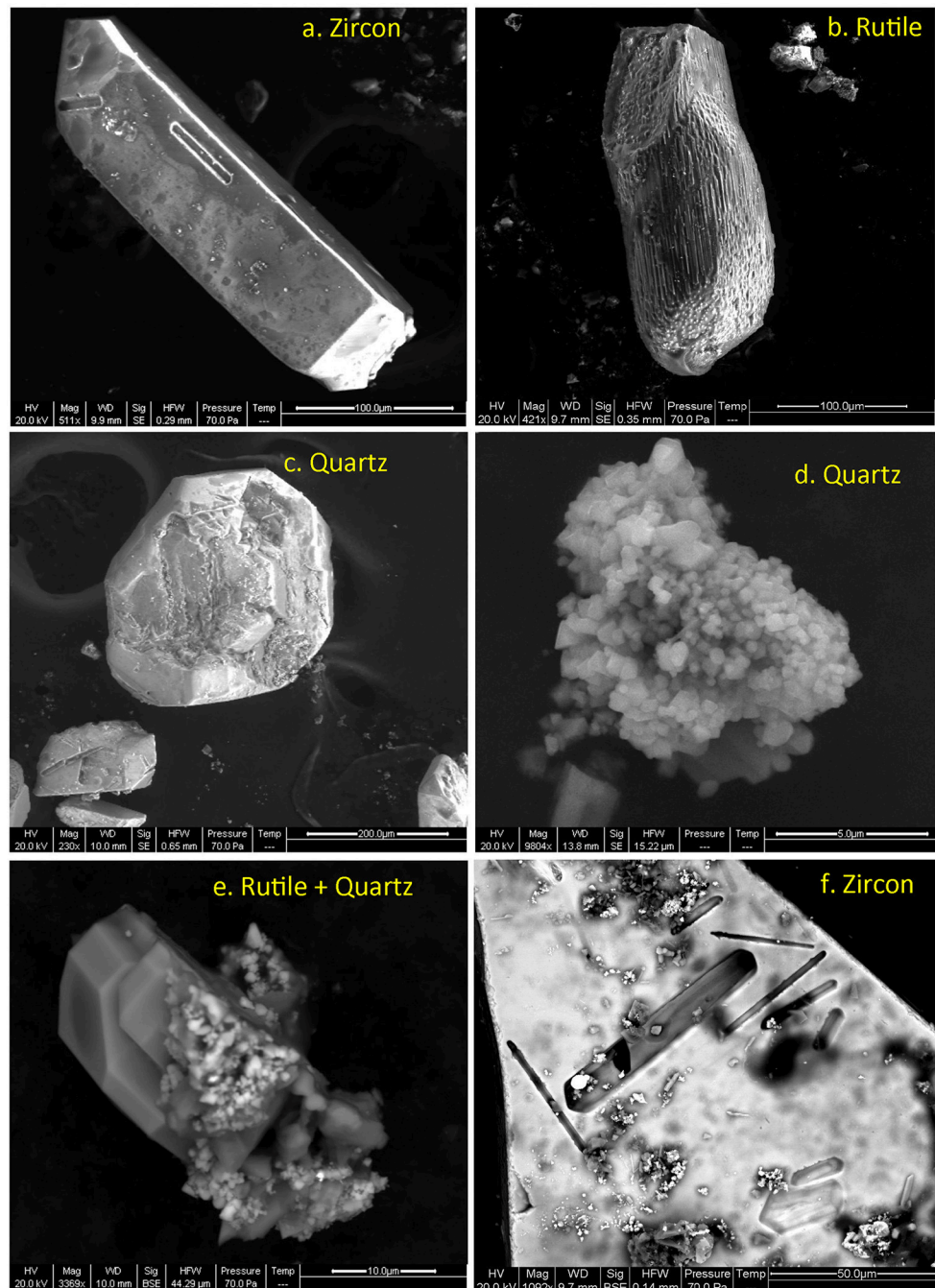
FIGURE 5 | Secondary electron images of extracted run products, prior to ultrasonic cleaning. **(a)** zircon, **(b)** rutile, **(c)** dissolved quartz, **(d)** secondarily precipitated quartz, **(e)** rutile with secondary quartz **(f)** magnified image of a zircon crystal face with pits left after dissolution of intergrown apatite which were exposed on the zircon surface.

clean without secondary quartz detectable by BSE and SE imaging. These crystals were used for surface profiling on the CAMECA ims 1270. Based on the detection of unexpectedly high enrichments in ^{18}O during SIMS frontside profiling (see below), crystals subsequently selected for TOF-SIMS and CAMECA 6f ion microprobe depth profiling were additionally twice immersed

in cold 20% HF solution for 30 s and ultrasonically rinsed in water to remove any remaining surface contamination. No visible changes of the crystal surfaces resulted from the brief HF wash under the microscope.

Crystals were pressed into indium metal alongside with starting MFT zircon grains using a polished tungsten carbide

anvil to align prism faces flush with the mount surface. Surfaces were further cleaned using ethanol and cotton swabs to remove dust under the microscope. Surface analysis of oxygen isotopes ($^{18}O/^{16}O$) by depth profiling was performed by two methods and instruments: magnetic sector SIMS using a CAMECA ims 1270 at University of California Los Angeles (UCLA) in frontside and backside depth profiling mode, and TOF-SIMS front side depth profiling using an ION-TOF Model IV at the University of Oregon. Depth profiling by either instrument record chemical or isotopic spikes with several atomic layer resolution (Hunter, 2009; Heber et al., 2014). Prior to analysis using the CAMECA ims 1270, mounts were Au coated, while TOF-SIMS measurements were performed without surface coating. The surfaces of samples studied by TOF-SIMS were additionally treated by 20% HF for 2 min twice directly on the indium mount prior to analysis and then washed with water and ethanol using cotton swabs. In addition to oxygen isotope analyses, we performed surface analyses for U-Pb in zircon by ims 1270 at UCLA, as well as depth profiling using a small magnet radius CAMECA ims 6f instrument at Arizona State University monitoring ^{18}O, ^{16}O, D, H, ^{6}Li, ^{7}Li, ^{11}B, and ^{10}B during the single run and present these results in Figures S1–S9 of the Supplementary Material.

Sample Preparation for Backside Depth Profiling

In order to verify results of the normal frontside depth profiles, we decided to examine surfaces using backside profiling, in which the original zircon crystal surface was approached from the interior outward (**Figure 3**). Such practice is common in the characterization of engineered semi-conductor materials, and is laborious and expensive. This technique avoids artificial profile broadening during analysis of thin-films, analogous to a highly ^{18}O-enriched surface layer on the experimentally treated zircon crystals. Because of the high cost of sample preparation, backside profiling was carried out only on one selected zircon crystal. This crystal was welded to a silicon wafer with platinum (**Figure 5**) and milled using the Focused Ion Beam (FIB) technique with a 30 kV and 40 nA Ga beam for 9 h. Ga ions impacting at shallow angle removed all zircon except for a ∼50 × 50 μm^2 zircon wafer with a thickness ∼3 μm (and a thickness range from 0.7–2 μm at the edges (**Figure 5b**; Figures S5, S10, S11 and Movie M1 in Supplementary Material). Using a micromanipulation needle, the zircon wafer was subsequently moved to a pristine silicon wafer where it was again welded in place using platinum.

SIMS Frontside and Backside Depth Profiling of Oxygen, H, Li, and B in Zircon

Multi-Collection Magnetic-Sector SIMS Profiles

Oxygen isotope analyses in frontside and backside profiling mode were conducted by multi-collection analysis using the UCLA CAMECA ims1270 (e.g., Trail et al., 2009); we only describe differences to these published procedures. To achieve homogeneous sputtering, a 20 keV total impact energy Cs^+ primary beam was slightly defocused to a ∼25 μm diameter

aperture-limited ("Köhler") illumination. Rastering of the primary beam (see below) was dismissed because of the necessity for charge compensation using a normal-incidence electron gun on an insulating material, which is difficult for a large sputtering area. Primary beam intensities were ∼5 nA (frontside profiling) and ∼1 nA (reverse profiling). To enhance depth resolution by limiting detection of ions from the periphery of the crater, two apertures were inserted into the secondary beam path: (1) the square field aperture was closed to a nominal width of 750 μm which would only admit ions from the inner ∼5 μm of the analysis spot into the mass spectrometer; and (2) the contrast aperture was narrowed to 150 μm to enhance spatial resolution. In combination, these settings decreased the secondary signal so that only ^{16}O could be detected on a Faraday cup (FC), whereas a Hamamatsu electron multiplier was used to simultaneously detect ^{18}O at intensities of ∼2–4 10^4 cps/nA Cs^+. All secondary ion intensities were corrected for FC backgrounds and EM dead time (65 ns). Instrumental mass fractionation (IMF), although of secondary importance given the large isotopic contrast between the natural zircon crystals and the experimental fluid charge, was corrected by analyzing reference zircon under the same analytical conditions as the unknowns. In the case of frontside profiles, reference zircon AS3 ($\delta^{18}O$ SMOW = +5.34‰; Trail et al., 2009) was analyzed in duplicate, whereas for backside profiling a single long run was conducted on a polished fragment of reference zircon 91500 ($\delta^{18}O$ SMOW = +9.9‰; Wiedenbeck et al., 2004). IMF ranged from 0.973 (backside profiling) to 0.980 (frontside profiling), which represents the normal variation in IMF during different analytical sessions. As a caveat, we note that the profile depth of reference zircon 91500 (∼1.3 μm) was significantly shallower than for the backside profile of the unknown (∼3 μm), but the largely invariant $\delta^{18}O$ for the unknown up to the point where the secondary beam drastically decreased due to sputtering through the zircon and into the underlying Si wafer suggests that there is no major change in IMF over the depth range analyzed here.

TOF SIMS Profiles

TOF-SIMS frontside depth profiles were acquired using a dual-beam method whereby a Cs^+ beam (2 kV, 54 nA, sputter area 400 × 400 μm^2, angle of incidence 45°, repetition rate 10 kHz) is used to excavate the crater, and a bismuth liquid metal ion source (25 kV Bi_3^+ primary ions, 0.3 pA, analysis area 125 × 125 μm^2, angle of incidence 45°, repetition rate 10 kHz) to generate mass spectra after each increment of Cs^+ sputtering. Charge neutralization was performed with a low-energy electron source in non-interlaced mode (5-s sputtering followed by 3-s pauses for charge neutralization). Excavation rates were determined by sputtering a single zircon crystal to a depth of ∼1 μm under identical beam conditions for several hours and measuring the resulting crater depth (see section Depth of Crater and Sputter Rate Measurements). Pixel selection for region-of-interest analysis of the ^{18}O distribution was accomplished by first creating chemical maps of the profile data and then selecting a region of uniform emission, being careful to avoid areas within several μm of the outer edges of the crystals (Kubicek et al., 2014).

Single-Collection Magnetic-Sector SIMS

Depth profiling on the ASU CAMECA ims 6f used a primary beam of $^{16}O_2^-$ (∼17 nA intensity) with an impact energy of 8.75 keV to sputter positive secondary ions from a 75 × 75 μm^2 crater, allowing only those ions originating from a circular area 15 μm across into the mass spectrometer. Zircons exposed to the isotopically labeled fluid as well as the starting zircon were examined for $^1H^+$, $^2H^+$, $^6Li^+$, $^7Li^+$, $^{10}B^+$, $^{11}B^+$ $^{18}O^+$, and $^{30}Si^+$ in peak-switching mode. When collecting the hydrogen isotopes and the silicon signal, a voltage offset was applied, so that only ions with 75 ± 20 eV excess kinetic energy were counted. This minimized the contribution of $^1H_2^+$ ions to the deuterium signal (Cherniak and Watson, 2010). No voltage offset was used during collection of the Li, B, and O ions to maximize the signal.

U-Pb Depth Profiling

In addition to oxygen isotopic depth profiling, short surface analyses were conducted for U-Pb isotopes in zircon using standard protocols for the UCLA CAMECA ims 1270 (e.g., Schmitt et al., 2003; Schmitt, 2009). Primary beam intensities for mass-filtered $^{16}O^-$ were ∼25 nA, and the secondary ion beam was transmitted essentially unrestricted by the field and contrast apertures. Although opening these apertures limits depth resolution, the resulting loss in secondary ion intensity would make the analyses meaninglessly imprecise. The purpose of these analyses was therefore not to detect potential diffusion profiles, but rather to test for mobility of Pb within the integrated analysis volume to a depth of ∼1 μm.

Depth of Crater and Sputter Rate Measurements

Correct determination of sputter rates is critical to establish accurate diffusion profiles. Depths of craters after magnetic sector SIMS and TOF-SIMS analysis were measured by optical interferometry using a MicroXAM profilometer. For this, we relied on measurements of ∼2 μm deep craters acquired under identical analytical conditions (ion beam incidence angle, primary beam energy and accelerating voltage) using large, polished crystal surfaces of reference zircons AS3 and 91500 (**Figure 9**). Sputtering rates for the conditions selected on the CAMECA ims 1270 are 0.4 nm/s/nA for Cs$^+$ and 0.14 nm/s/nA for O$^-$. Ion beam mixing can affect depth resolution. We monitored this by analyzing Au (from the conductive surface coating) under conditions of Cs$^+$ sputtering, and determined a decay length (reduction of intensity by a factor of e) of ∼38 nm.

RESULTS

Dynamic SIMS Frontside Profiling for δ^{18}O

Four frontside profiles on ZE1 zircon and one profile of the original MFT starting zircon material were acquired (**Figure 7**). In three measured profiles (ZE1, z1, 2, and 4, **Figure 7**) high δ^{18}O values persisted to ∼120 nm depth, showing a decline in secondary ion intensity for ^{18}O similar to Au from the surface coating analyzed under the same conditions. Zircon profile ZE1 z3 shows an initial decline, followed by an intermittent increase in ^{18}O. At ca. ∼140 nm depth, the ^{18}O signal decayed to background

levels. Untreated MFT zircon yielded flat intensity profiles, and homogeneous δ^{18}O values (**Figure 7**). Error function fitting of the depth profiles results in poor matches for all four profiles (Figure S9, Supplementary Material). Moreover, the similarity between the δ^{18}O profiles and that for Au (**Figure 7**) is suspicious, and hints at secondary ion induced mixing of surface-enriched ^{18}O into deeper crystal domains instead of Fickian volume diffusion (**Figure 1**), as is discussed below.

SIMS Backside Profiling for δ^{18}O

The combination of suspected residual ^{18}O-rich material deposited on zircon crystal surfaces after the experiment and the likely short diffusion profile led us to carry out backside profiling, a method rarely used in Earth Science applications (cf. Heber et al., 2014). A selected ZE1 zircon crystal thinned by FIB (**Figure 6**) showed an initial 200 nm interval of increasing oxygen secondary ion signal, followed by a steady decrease in ^{18}O, explained by varying ionization conditions, while δ^{18}O remained invariant within analytical uncertainty (**Figure 8**). Only after the oxygen secondary ion signal dropped dramatically ∼3 μm deep into the profile, δ^{18}O increased significantly. A mechanically polished fragment of 91500 reference zircon was run under the same conditions; the profile differs in that the depth of initial signal stabilization was much shallower than for the crystal prepared by FIB. Subsequently, the oxygen secondary ion intensity remained constant to ca. 400 nm depth and then gradually decreased to the final profile depth of 1.3 μm. Over the entire 91500 zircon profile, δ^{18}O decreased gradually by 2–3‰.

From comparison of the two profiles, we conclude that the original crystal surface was breached in backside profiling at a depth of ∼3 μm, as indicated by the sharp decline in secondary ion intensity. Subsequent inspection of the crater shows that the crystal was cracked in the crater area (**Figure 9**). Although a crack was initially visible at the margin of the crystal, ion imaging prior to analysis revealed no intensity anomaly for the region sampled by the field aperture (**Figure 9**). It is thus likely that the crack was encountered at depth, which may explain the gradual decline of the secondary ion intensity over the last 200 nm of the profile, instead of a sharp drop. Regardless of this complexity, δ^{18}O values remained constant, with no measureable increase even for the last 100 nm before breaching the surface for which an increase to +450 ‰ would be predicted.

TOF SIMS Frontside Profiling

TOF-SIMS frontside profiles were performed on zircon surfaces from ZE1, ZE2, and untreated MFT in two sessions (**Figure 10**). Sputter rates at ∼0.12 nm/s for TOF-SIMS acquisition were much lower than for the conditions chosen for magnetic sector SIMS, and targeted the outermost and uncoated crystal surfaces. ^{18}O ion intensities were normalized to the major ion $^{90}ZrO^+$ to correct for variations in secondary ion intensities. In both exchange experiment zircons (ZE1, ZE2) and starting MFT zircons, ^{18}O intensities are enhanced in the outermost 1–2 nm (**Figure 10B**); we consider this to be an artifact of ion intensity stabilization during surface analysis. However, MFT $^{18}O/^{90}ZrO^+$ intensity ratios level out to a constant value, whereas the ZE1 zircon profiles continue to exhibit elevated $^{18}O/^{90}ZrO^+$ ratios to
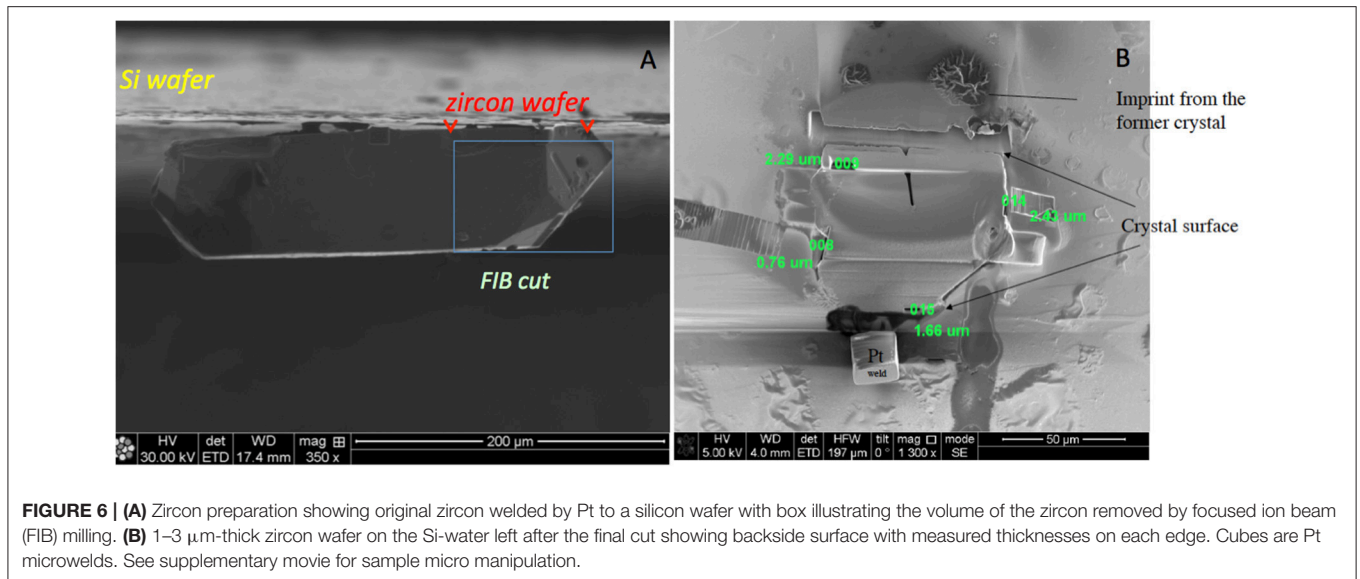
FIGURE 6 | (A) Zircon preparation showing original zircon welded by Pt to a silicon wafer with box illustrating the volume of the zircon removed by focused ion beam (FIB) milling. **(B)** 1–3 μm-thick zircon wafer on the Si-water left after the final cut showing backside surface with measured thicknesses on each edge. Cubes are Pt microwelds. See supplementary movie for sample micro manipulation.
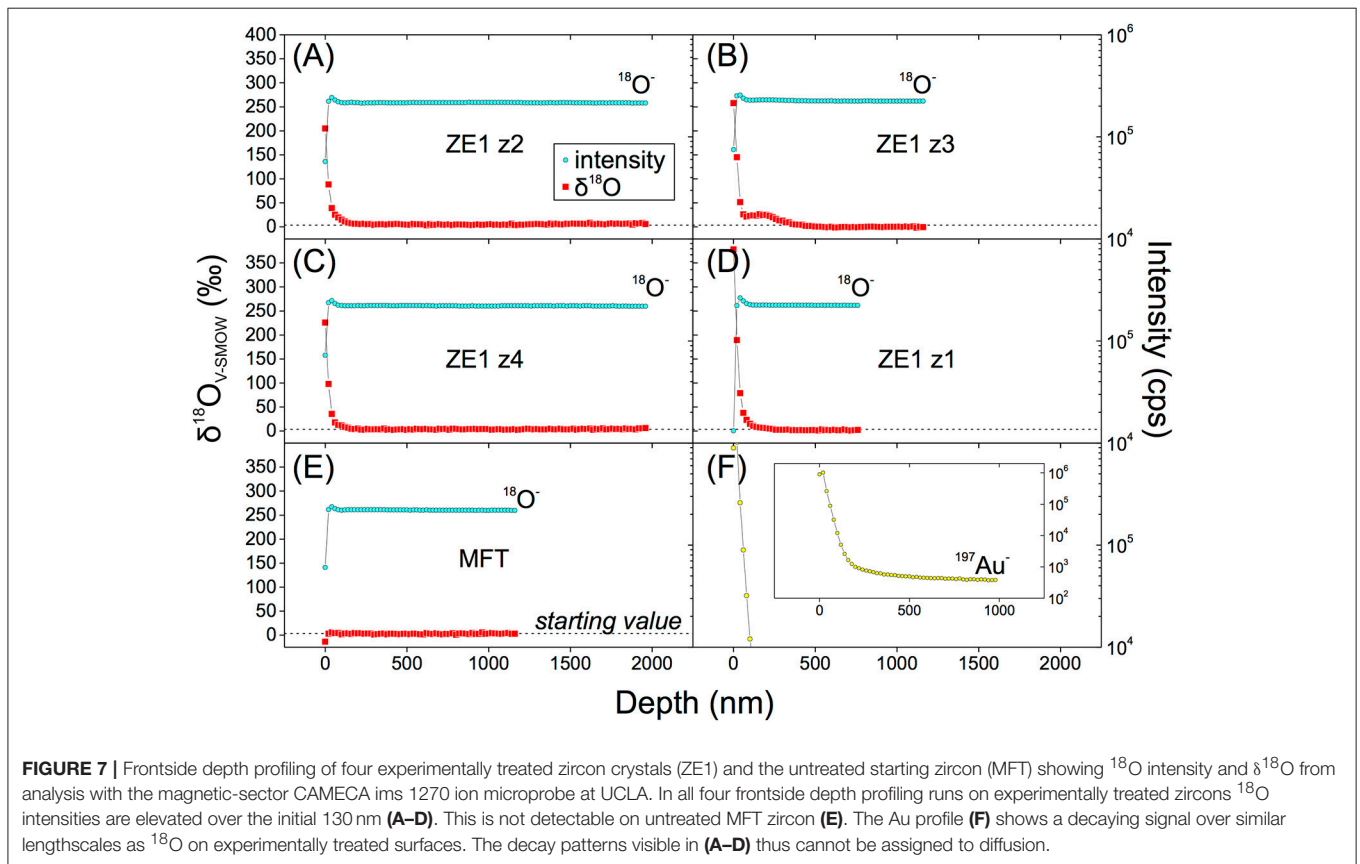

FIGURE 7 | Frontside depth profiling of four experimentally treated zircon crystals (ZE1) and the untreated starting zircon (MFT) showing ^{18}O intensity and $\delta^{18}O$ from analysis with the magnetic-sector CAMECA ims 1270 ion microprobe at UCLA. In all four frontside depth profiling runs on experimentally treated zircons ^{18}O intensities are elevated over the initial 130 nm **(A–D)**. This is not detectable on untreated MFT zircon **(E)**. The Au profile **(F)** shows a decaying signal over similar lengthscales as ^{18}O on experimentally treated surfaces. The decay patterns visible in **(A–D)** thus cannot be assigned to diffusion.

~15 nm depth. ZE2 zircon surfaces also exhibit rapidly decaying ^{18}O enhancement over the first several nm but become similar to MFT at shallower depths (~20 nm) relative to ZE1 zircon. It appears that measurable exchange of oxygen between fluid and zircon has occurred regardless of the length of exposure and at a maximum of 20 nm length-scale.

Large Magnet Radius SIMS U-Pb Age Analysis

Surface U-Pb zirconanalyses were carried out for seven ZE1 and four untreated MFT zircon faces, with a depth penetration of ~2 μm for a ca. 11 min analysis. Following corrections for common Pb based on measured ^{207}Pb, and initial ^{230}Th
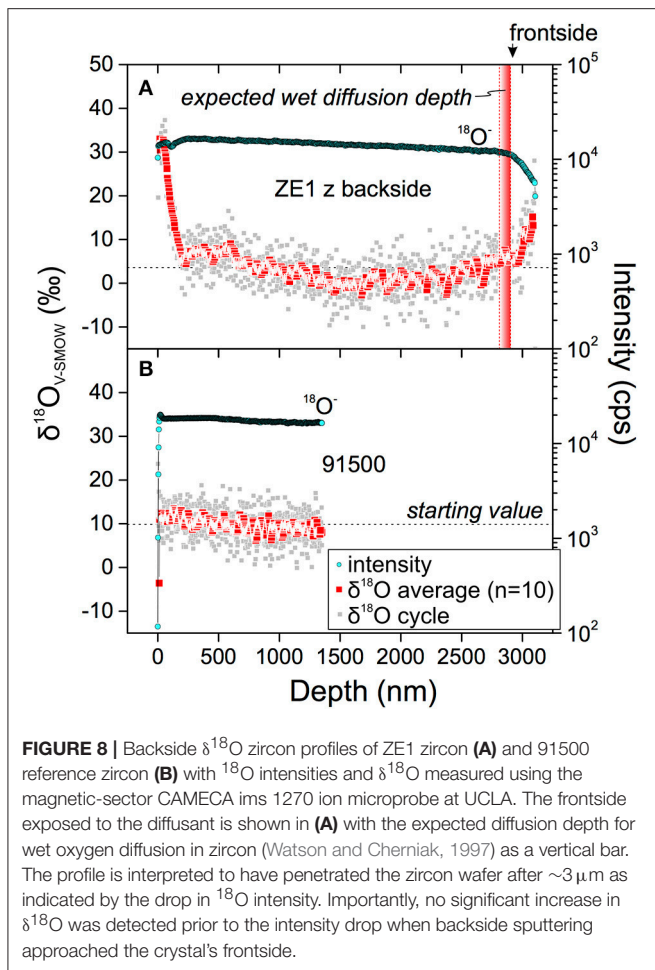
FIGURE 8 | Backside $\delta^{18}O$ zircon profiles of ZE1 zircon **(A)** and 91500 reference zircon **(B)** with ^{18}O intensities and $\delta^{18}O$ measured using the magnetic-sector CAMECA ims 1270 ion microprobe at UCLA. The frontside exposed to the diffusant is shown in **(A)** with the expected diffusion depth for wet oxygen diffusion in zircon (Watson and Cherniak, 1997) as a vertical bar. The profile is interpreted to have penetrated the zircon wafer after ~3 μm as indicated by the drop in ^{18}O intensity. Importantly, no significant increase in $\delta^{18}O$ was detected prior to the intensity drop when backside sputtering approached the crystal's frontside.

disequilibrium, both sets of ages are identical within analytical uncertainties (ZE1: 1.36 ± 0.12 Ma, MSWD = 0.22, $n = 7$; MFT: 1.22 ± 0.10 Ma, MSWD = 0.18, $n = 4$). Subsequent analyses in the same spots of ZE1 zircons to a total depth of 6 μm yielded identical ages which are within error of the currently accepted 1.30 Ma Ar/Ar age of MFT (Lanphere et al., 2002; Rivera et al., 2016). This result suggests lack of any appreciable Pb loss or gain even in the outermost layers of zircons after 4 months in silica-saturated solution at 850°C (**Figure 11**) at estimated ~10% level of propagated uncertainty.

Small Magnet Radius SIMS (CAMECA ims 6f) Depth Profiling Analyses and Qualitative Observations

H and D/H

Both MFT and ZE1 zircons show initially high H intensities, which dropped at the same rate with depth (Supplementary Material, Figures S2–S5). We interpret high initial intensities of H^+ as contamination present on the zircon crystal surfaces. After sputtering ~150–200 nm deep, a steady H^+ intensity was reached which may approach the contribution of H intrinsic to background. The H^+ signal in experimental ZE1 zircon was

always higher than for untreated MFT zircon, whereas the $^{30}Si^+$ signal was nearly the same. The elevated hydrogen signal in the ZE1 zircon also persisted to the end of the depth profiling experiment to ~1–1.5 μm depth, suggesting ~4× higher overall hydrogen concentrations in ZE1 zircon compared to untreated MFT zircon. No D^+ was analytically detected above the 1 count per second threshold even at the shallow surface, suggesting that despite doping with water having $\delta D = +350‰$, no measurable migration of deuterium from the fluid into the crystal occurred.

Li and B Abundances

Both ZE1 and MFT zircon crystals show elevated intensities of Li near the surface (**Figure 12**), possibly due to surface contamination, but Li intensities are two to three orders of magnitude higher in ZE1 zircon than in MFT zircon throughout the profile. The Li depth profile shows a hump-shaped profile with irregular minor increases at depths between ~50 and ~200 nm; it cannot be reliably fit by an error function expected for Fickian diffusion. Profiles for $^{10}B^+$ and $^{11}B^+$ mimic the Li profile, suggesting identical migration mechanisms for boron and lithium. Compared with Li intensity changes between ZE1 and MFT, B intensity is elevated by one order of magnitude in ZE1 zircon compared to the MFT zircon. Very high initial B and Li concentrations in ZE1 and MFT zircons in the very beginning of the profiles is a combination of frontside profile artifacts and/or surficial contamination.

$^7Li/^6Li$ and $^{11}B/^{10}B$

Plotting Li and B isotopic values vs. depth (Figure S5) shows a gradual increase in $^7Li/^6Li$ from ~12 to 13, which then steadies out at an average $^7Li/^6Li$ ratio of 13.4. The $^{11}B/^{10}B$ ratio remains constant at 3.54 over the entire depth range. If an instrumental mass bias calibration for lithium and boron isotopes on clay minerals is used (which was obtained a few minutes after these depth profiles were completed), the measured ratios would imply $\delta^7Li \sim +70‰$ and $\delta^{11}B \sim -70‰$. Elevated δ^7Li over the entire profile length is consistent with uptake of lithium via fast diffusion pathways likely micro-cracks. Boron, however, approaches $\delta^{11}B$ values typical for untreated MFT zircon in 2000 sec (~200 nm).

$^{18}O/^{16}O$

Frontside profiling for oxygen on ZE1 and MFT zircons shows initially elevated intensities of mass 18 near the surface. Intensities return to a steady value from a depth of ~20–25 nm on (Figure S8). The initially elevated intensity could be due to interference with H_2O^+ (in line with **Figure 9** of TOF-SIMS profiling) which would not have been resolved in the high transmission-low mass resolution tuning of the CAMECA ims 6f. There could also be a contribution from incompletely removed surface residues to the initially elevated $^{18}O^+$ signal. Regardless, the rapid decay of the $^{18}O^+$ signal at the beginning of the profile can only be reconciled with an extremely short diffusion length-scale of <20–25 nm.
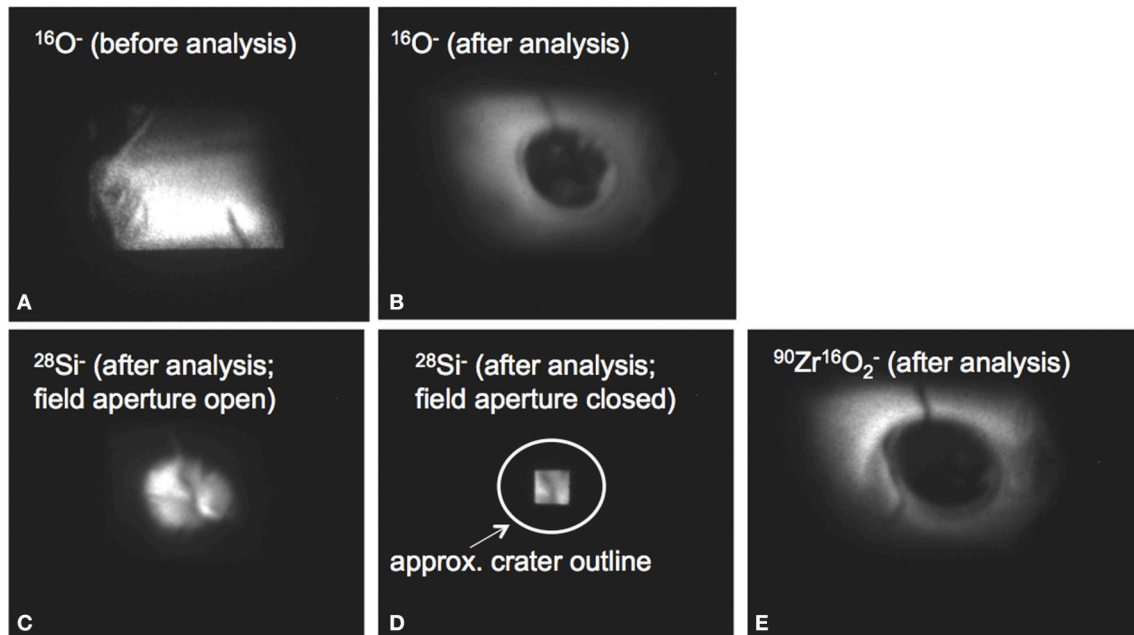
FIGURE 9 | Direct secondary ion images of the analyzed area of ZE1 zircon before and after the backside depth profile generated with a $75 \times 75 \, \mu m^2$ rastered beam. Ion images were recorded on the channel plate detector of the CAMECA ims 1270. **(A)** ^{18}O image of the ZE1 target area before analysis with field aperture open. Note crack in crystal in the SE corner, which is not visible in the center analyzed during depth profiling. **(B)** ^{18}O image after depth profiling. Central hole shows crater $\sim$30 μm in diameter. **(C)** ^{28}Si image after depth profiling. High intensity in the crater is due to sputtering of the silicon wafer substrate. **(D)** ^{28}Si image after depth profiling as in **(C)** but with field aperture closed to demonstrate sampling of ions only from a $5 \times 5 \, \mu m^2$ area in the interior of the crater. **(E)** $^{90}Zr^{16}O_2$ image after depth profiling showing complete penetration of zircon in the crater.

DISCUSSION AND IMPLICATIONS

This work describes novel approaches to measure isotopic zoning with extremely high spatial resolution that can now be added to the zircon researchers toolbox. Our study demonstrates that very slow diffusion rates through zircon occur when immersed in hydrothermal solution, with undetectable diffusion of oxygen over the course of a 4-month duration experiment at 850°C and 50 MPa. TOF-SIMS depth profiling suggests minor ^{18}O enrichment within the outermost 1–10 nm of zircon crystal surfaces exposed to the fluid, but it remains unresolved if this is due to diffusion, solution-reprecipitation, or incomplete removal of surficial contaminants. Even if this did reflect diffusion, the diffusive length-scale would be on the order of 1–10 nm, equivalent to only 10–100 atomic layers, with corresponding D on the order of $1–3 \times 10^{-23}$ m^2/s. Such values would be more consistent with the "dry" diffusion coefficients of Watson and Cherniak (1997), but not with the "wet" hydrothermal conditions the zircons were subjected to in the experiment. Note that solution became effectively doped with an excess of 206Pb after dissolution of 1.87 Ga rutile (**Figure 5b**).

Our study also suggests that depth profiles produced by ion microprobe frontside surface analysis of shallow (<100 nm) layers reflect the effects of ion beam mixing known from thin-film analysis of synthetic semiconductor materials (e.g., Williams and Baker, 1981; Hunter, 2009). Ion beam mixing leads to a work-in/implanting of surface impurities, generating pseudo-diffusion profiles; for example, we observe a profile of decreasing Au

intensity with depth which cannot reflect diffusion, but instead results from ion mixing of the conductive Au coating deposited onto the surface (**Figure 7**). Ion collisions between primary beam ions and surface ions can lead to higher concentrations of very enriched surface layer ions in the topmost 10 s of nm where ions are displaced upward or downward relative to their original position within the collision cascade triggered by energetic primary ion impacts. Likewise, H_2O contamination of the surface from residual gases even in the high vacuum may causes initially higher apparent abundances of ^{18}O on reacted and unreacted surfaces during initial sputtering; however, these isobaric interferences are only critical if unresolved at low mass resolution.

In contrast to frontside analysis, magnetic-sector SIMS backside profiling resulted in nearly constant $\delta^{18}O$ values. This provides additional evidence for essentially no diffusion of isotopically spiked oxygen into zircon during the experiment. Based on the backside profiling, we interpret the initially elevated ^{18}O signals in both TOF-SIMS and magnetic-sector SIMS frontside profiling as analytical artifacts because: (1) the ^{18}O profile appears similar to that of Au deposited onto the surface; (2) ^{18}O profiles are indistinguishable between long-term and "zero-time" crystals; and (3) elements with very different expected diffusivities (e.g., H, Li, B, and O) display similar profiles.

Diffusion of Li and B (**Figure 12**) cannot be explained by Fickian behavior. This agrees with evidence for slow and fast diffusion pathways for Li in zircon from natural samples (Tang
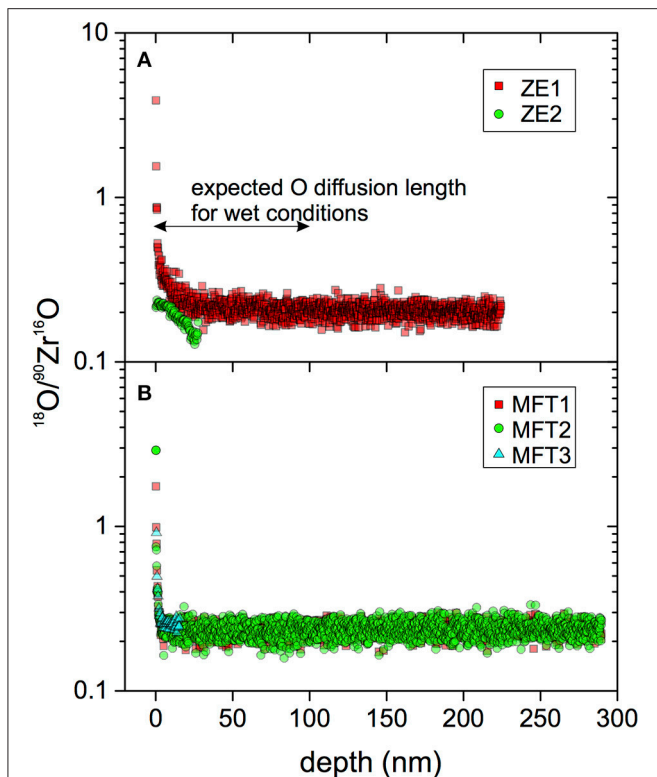
FIGURE 10 | TOF-SIMS frontside depth profiling of zircons from (A) long term (4 months, ZE1) and short term (1 day, ZE2) experiments and (B) concurrently run starting material MFT. The ^{18}O intensity is normalized to the ZrO secondary ion intensity to minimize variations due to sputtering instability, and a sputter rate of 0.12 nm/s is used to convert time to depth Transient initial (over ~2 nm) high values of ^{18}O/ZrO are common to all depth profiles generated here, and thus do not reflect abundance variations of ^{18}O. Experimentally treated zircon ZE1 and ZE2 have a more protracted ^{18}O/ZrO decay over ~15 nm. Because this is present also in the short-term experiment, this decay is not due to diffusion but likely to the presence of a very thin ^{18}O-enriched surface layer. Regardless, no enrichment in ^{18}O was found over the length-scales relevant for wet diffusion of oxygen (arrow).
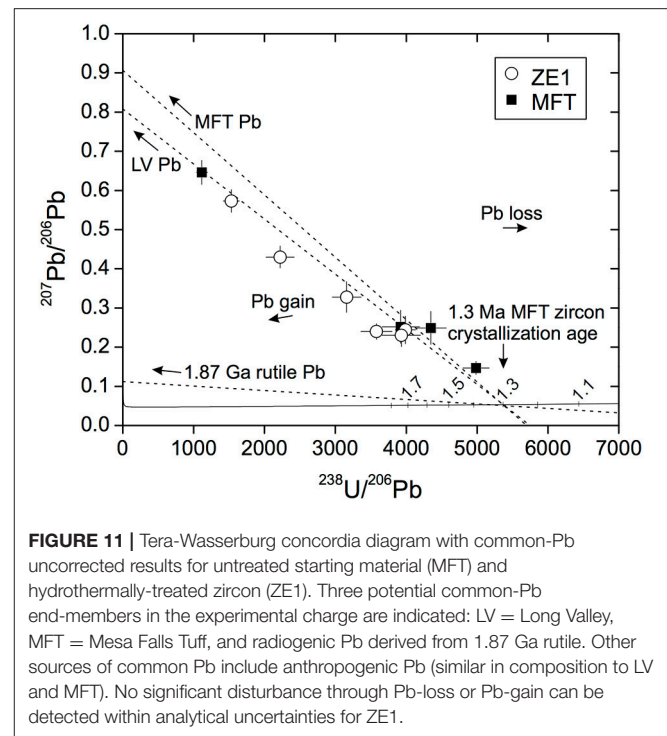
FIGURE 11 | Tera-Wasserburg concordia diagram with common-Pb uncorrected results for untreated starting material (MFT) and hydrothermally-treated zircon (ZE1). Three potential common-Pb end-members in the experimental charge are indicated: LV = Long Valley, MFT = Mesa Falls Tuff, and radiogenic Pb derived from 1.87 Ga rutile. Other sources of common Pb include anthropogenic Pb (similar in composition to LV and MFT). No significant disturbance through Pb-loss or Pb-gain can be detected within analytical uncertainties for ZE1.

et al., 2017). Slow diffusion could be coupled to rare earth element (REE) and Y abundance or possibly other trivalent cations (e.g., Al), whereas fast diffusion appears to be independent of REE+Y in the zircon lattice (Tang et al., 2017). Our experiments, in particular the hump shaped profile for Li, underscores the presence of multiple diffusion pathways. Although analytical procedures were not designed to determine Pb diffusion, our results find no evidence for Pb-loss or gain during the 4-month duration experiment, and agree with very small Pb diffusion coefficients previous determined for crystalline zircon (Cherniak and Watson, 2001).

Our study has implications for survivability of oxygen and Pb isotopes in zircon in hot silica-saturated hydrothermal solutions. Studies by Peck et al. (2003), Chen et al. (2003), Page et al. (2007), Bowman et al. (2011) and Bindeman et al. (2014) used metamorphic overgrowths of different age and variably contrasting $\delta^{18}O$ values to demonstrate preservation of steep profiles in high-grade (T >750°C) metamorphic rocks

(Figure 2). The apparent robustness of zircon's isotopic and trace elemental information (e.g., Wilde et al., 2001; Cavosie et al., 2006; Harrison et al., 2008; Spencer et al., 2017) is reassuring and lends confidence to extracting reliable geologic information from detrital grains where geologic and thermal histories remain unknown (Maas and McCulloch, 1991). It appears that only very protracted residence at very high T (>800°C), or a solution-reprecipitation would be able to erase the original oxygen isotopic information in zircon (e.g., Valley, 2003). An important caveat of our and previous experiments is that the extremely slow isotopic exchange should only be considered valid for crystalline zircon, whereas metamict zircon appears to be much more reactive in the presence of hydrothermal fluids, for example leading to depletion in oxygen isotopic compositions with concomitant Pb-loss and discordance (e.g., Booth et al., 2005; Roberts et al., 2018).

Our study demonstrates diffusion much slower than predicted from experiments in Watson and Cherniak (1997). In our hydrothermal experiments, intracrystalline exchange of oxygen between fluid and zircon occurred over length-scales equivalent to those predicted for dry diffusion with D ≤ 1–3×10^{-23} m^2/s at 850°C, underscoring a virtual lack of oxygen diffusion and an outstanding survivability of zircons and its isotopic inventory under most metamorphic and hydrothermal conditions.

Future effort and experimentation should target investigation of microcracks on diffusion as a mechanism for fast exchange. Additional investigation of metamict and partially-metamict zircons in controlled experiments will extend the results of current work as experiments are easier to reliably interpret than studies of natural materials. For this purpose, we recommend using natural and not artificially-perfect synthetic, or even kimberlitic, zircons for experimental work. Such experimental
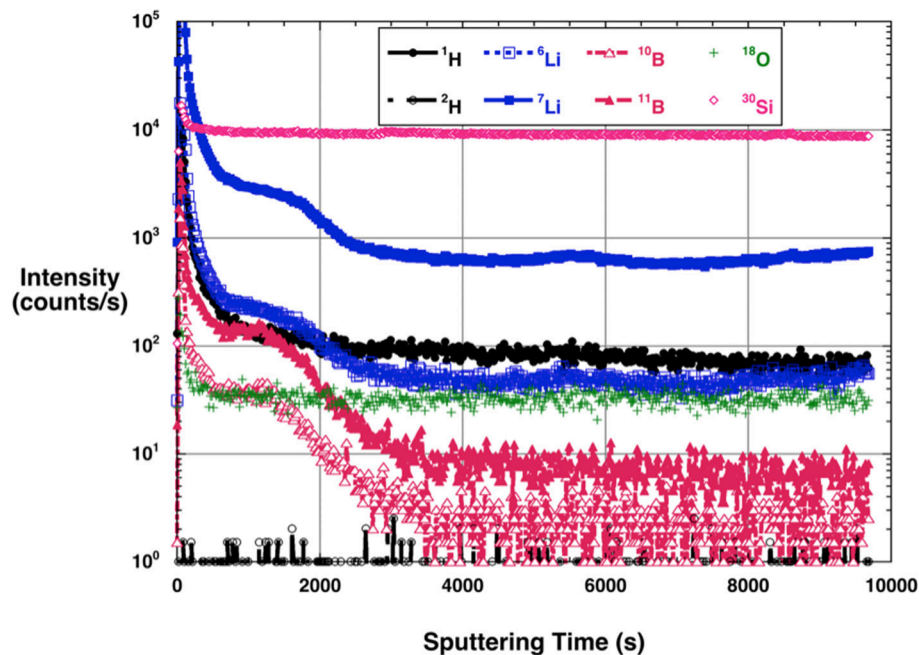
FIGURE 12 | Profile monitoring the isotopes of H, Li, and B (as well as $^{18}O^+$ and $^{30}Si^+$) with depth into a ZE1 experiment zircon held at 850°C for 4 months. See Supplementary figures for concurrently run MFT starting material and isotopic ratios profiles. Total depth acquired during this analysis run is in between 1 and 1.6 micrometers. "Snowplow" shape of the profile between 800 and 3,000 s is explained by inadvertently overlapping a crack filled with trace non-volatile elements Li and B. This did not affect major elements. High ^{18}O signal persists for ~400 s or 30 nm but twice as long for H. $^2H(D)$ is below detection. High ^7Li and ^{10}B is due to doping the experimental solution with these elements.

studies using natural zircons will add to clarifying the mobility of oxygen, water, lithium, boron, lead and other elements in diverse set of zircon samples from nature. We also recommend careful characterization of microcracks and history of microcracking in natural zircons, as well as the degree of metamictization at an appropriate sub-micrometer scale, although we recognize that such approaches would be challenging to be implemented in routine natural zircon studies.

AUTHOR CONTRIBUTIONS

IB conceived the study, prepared samples for analyses and wrote the paper; AS performed all CAMECA 1270 SIMS measurements; CL conducted the hydrothermal experiment; RH performed CAMECA 7f measurements. All authors edited the paper.

SUPPLEMENTARY MATERIAL

The Supplementary Material for this article can be found online at: https://www.frontiersin.org/articles/10.3389/feart. 2018.00059/full#supplementary-material

REFERENCES

Abramov, O., and Kring, D. A. (2005). Impact-induced hydrothermal activity on early *Mars. J. Geophys. Res.* 110:E12SO9. doi: 10.1029/2005JE002453

Abramov, O., Kring, D. A., and Mojzsis, S. J. (2013). The impact environment of the Hadean Earth. *Chemie der Erde* 73, 227–248. doi: 10.1016/j.chemer.2013.08.004

Audètat, A., and Keppler, H. (2005). Solubility of rutile in subduction zone fluids, as determined by experiments in the hydrothermal diamond anvil cell. *Earth Planet. Sci. Lett.* 232, 393–402. doi: 10.1016/j.epsl.2005.01.028

Ayers, J. C., and Watson, E. B. (1991). Solubility of apatite, monazite, zircon, and rutile in supercritical aqueous fluids with implications for

subduction zone geochemistry. *Phil. Trans. R. Soc. Lond.* 335, 365–375. doi: 10.1098/rsta.1991.0052

Ayers, J. C., and Watson, E. B. (1993). Rutile solubility and mobility in supercritical aqueous fluids. *Contrib. Mineral. Petrol.* 114, 321–330. doi: 10.1007/BF01046535

Ayers, J. C., Zhang, L., Luo, Y., and Peters, T. J. (2012). Zircon solubility in alkaline aqueous fluids at upper crustal conditions. *Geochim. Cosmochim. Acta* 96, 18–28. doi: 10.1016/j.gca.2012.08.027

Bernini, D., Audetat, A., Dolejs, D., and Keppler, H. (2013). Zircon solubility in aqueous fluids at high temperatures and pressures. *Geochim. Cosmochim. Acta* 119, 178–187. doi: 10.1016/j.gca.2013.05.018

Bindeman, I. N., Fu, B., Kita, N., and Valley, J. W. (2008). Origin and evolution of yellowstone silicic magmatism based on the ion microprobe analysis of isotopically-zoned zircons. *J. Petrol.* 49, 163–193. doi: 10.1093/petrology/egm075

Bindeman, I. N., Serebryakov, N. S., Schmitt, A. K., Vazquez, J., Guan, Y., Astafiev, B., et al. (2014). Field and microanalytical isotopic investigation of ultra-depleted in 18-O Paleoproterozoic "Slushball Earth" rocks from Karelia, Russia. *Geosphere* 10, 308–339. doi: 10.1130/GES00952.1

Bindeman, I. N., and Simakin, A. G. (2014). Rhyolites - hard to produce but easy to recycle and sequester: bringing together microgeochemical observations and numerical models. *Geosphere* 10, 930–957. doi: 10.1130/GES00969.1

Bindeman, I. N., and Valley, J. W. (2002). Oxygen isotope study of the Long Valley magma system, California: isotope thermometry and convection in large silicic magma bodies. *Contrib. Mineral. Petrol.* 144, 185–205. doi: 10.1007/s00410-002-0371-8

Booth, A. L., Kolodny, Y., Chamberlain, C. P., McWilliams, M., Schmitt, A. K., and Wooden, J. (2005). Oxygen isotopic composition and U-Pb discordance in zircon. *Geochim. Cosmochim. Acta* 69, 4895–4905. doi: 10.1016/j.gca.2005.05.013

Bowman, J. R., Moser, D. E., Valley, J. W., Wooden, J. L., Kita, N. T., and Mazdab, F. K. (2011). Zircon U-Pb isotope, $\delta^{18}O$ and trace element response to 80 My of high temperature metamorphism in the lower crust: sluggish diffusion and new records of Archean craton formation. *Am. J. Sci.* 311, 719–772. doi: 10.2475/09.2011.01

Cavosie, A. J., Valley, J. W., and Wilde, S. A. (2006). Correlated microanalysis of zircon: trace element, $\delta^{18}O$, and U-Th-Pb isotopic constraints on the igneous origin of complex >3900 Ma detrital grains. *Geochim Cosmochim Acta* 70, 5601–5616. doi: 10.1016/j.gca.2006.08.011

Chen, D., Deloule, E., Cheng, H., Xia, Q., and Wu, Y. (2003). Preliminary study of microscale zircon oxygen isotopes for Dabie-Sulu metamorphic rocks: ion probe *in situ* analyses. *Chin. Sci. Bull.* 48, 1670–1678. doi: 10.1360/03wd0037

Cherniak, D. J., and Watson, E. B. (2001). Pb diffusion in zircon. *Chem. Geol.* 172, 5–24. doi: 10.1016/S0009-2541(00)00233-3

Cherniak, D. J., and Watson, E. B. (2010). Li diffusion in zircon. *Contrib. Mineral. Petrol.* 160, 383–390. doi: 10.1007/s00410-009-0483-5

Claesson, S., Bibikova, E. V., Shumlyanskyy, L., Whitehouse, M. J., and Billströma, K. (2016). Can oxygen isotopes in magmatic zircon be modified by metamorphism? A case study from the Eoarchean Dniester-Bug Series, Ukrainian Shield. *Precambrian Res.* 273, 1–11. doi: 10.1016/j.precamres.2015.11.002

Fournier, R. O. (1985). The behavior of silica in hydrothermal solutions. *Rev. Econ. Geol.* 2, 45–61.

Hanchar, J. M., and Hoskin, P. W. O. (2003). *Zircon*. Chantilly, VA: Mineralogical Society of America.

Harrison, T. M. (2009). The Hadean crust: evidence from> 4 Ga zircons. *Annu. Rev. Earth Planet. Sci.* 37, 479–505. doi: 10.1146/annurev.earth.031208.100151

Harrison, T. M., Schmitt, A. K., McCulloch, M. T., and Lovera, O. M. (2008). Early (≥4.5 Ga) formation of terrestrial crust: Lu-Hf, $\delta^{18}O$, and Ti thermometry results for Hadean zircons. *Earth Planet. Sci. Lett.* 268, 476–486. doi: 10.1016/j.epsl.2008.02.011

Heber, V. S., McKeegan, K. D., Burnett, D. S., Duprat, J., Guan, Y., Jurewicz, A. J., et al. (2014). Accurate analysis of shallowly implanted solar wind ions by SIMS backside depth profiling. *Chem. Geol.* 390, 61–73. doi: 10.1016/j.chemgeo.2014.10.003

Hunter, J. L. (2009). "Improving depth profile measurements of natural materials: lessons learned from electronic materials depth-profiling," in *Secondary Ion Mass Spectrometry in the Earth Sciences: Gleaning the Big Picture From a Small Spot*, Vol. 41, ed M. Fayek (Toronto, ON: Mineralogical Association of Canada), 133–148.

Kubicek, M., Holzlechner, G., Opitz, A. K., Larisegger, S., Hutter, H., and Fleig, J. (2014). A novel ToF-SIMS operation mode for sub 100 nm lateral resolution: application and performance. *Appl. Surf. Sci.* 289, 407–416. doi: 10.1016/j.apsusc.2013.10.177

Lanphere, M. A., Champion, D. E., Christiansen, R. L., Izett, G. A., and Obradovich, J. D. (2002). Revised ages for tuffs of the Yellowstone plateau volcanic field: assignment of the Huckleberry Ridge Tuff to a new geomagnetic polarity event. *Geol. Soc. Am. Bull.* 114, 559–568. doi: 10.1130/0016-7606(2002)114andlt;0559:RAFTOTandgt;2.0.CO;2

Maas, R., and McCulloch, M. T. (1991). The provenance of Archean clastic metasediments in the Narryer gneiss complex, Western Australia: trace element geochemistry, Nd isotopes, and U-Pb ages from detrital zircons. *Geochim. Cosmochim. Acta* 55, 1915–1932. doi: 10.1016/0016-7037(91)90033-2

Manning, C. E., Wilke, M., Schmidt, C., and Cauzid, J. (2008). Rutile solubility in albite-H_2O and $Na_2Si_3O_7$-H_2O at high temperatures and pressures by *in situ* synchrotron radiation micro-XRF. *Earth Planet. Sci. Lett.* 272, 730–737. doi: 10.1016/j.epsl.2008.06.004

Melnik, O. E., and Bindeman, I. N. (2018). Modeling of trace elemental zoning patterns in accessory minerals with emphasis on the origin of micrometer-scale oscillatory zoning in zircon. *Am. Mineral.* 103, 355–368. doi: 10.2138/am-2018-6182

Page, F. Z., Ushikubo, T., Kita, N. Y., Riciputi, L. R., and Valley, J. W. (2007). High precision oxygen isotope analysis of picogram samples reveals 2-mm gradients and slow diffusion in zircon. *Am. Mineral.* 92, 1772–1775. doi: 10.2138/am.2007.2697

Peck, W. H., Valley, J. W., and Graham, C. M. (2003). Slow oxygen diffusion rates in igneous zircons from metamorphic rocks. *Am. Mineral.* 88, 1003–1014. doi: 10.2138/am-2003-0708

Reed, D. J., and Wuensch, B. J. (1980). Ion-probe measurement of oxygen self-diffusion in single-crystal Al_2O_3. *J. Am. Ceram. Soc.* 63, 88–92. doi: 10.1111/j.1151-2916.1980.tb10655.x

Rivera, T. A., Schmitz, M. D., Jicha, B. R., and Crowley, J. L. (2016). Zircon petrochronology and $^{40}Ar/^{39}Ar$ sanidine dates for the mesa falls tuff: crystal-scale records of magmatic evolution and the short lifespan of a large yellowstone magma chamber. *J. Petrol.* 57, 1677–1704. doi: 10.1093/petrology/egw053

Roberts, N. M. W., Yang, Q. Y., and Santosh, M. (2018). Rapid oxygen diffusion during high temperature alteration of zircon. *Nat. Sci. Rep.* 8:3661 doi: 10.1038/s41598-018-22016-2

Rubatto, D. (2017). Zircon: the metamorphic mineral. *Rev. Mineral. Geochem.* 83, 261–295. doi: 10.1515/9783110561890-010

Schaltegger, U. (2007). Zircon tiny but timely: hydrothermal zircon. *Elements* 3, 51–79. doi: 10.2113/gselements.3.1.51

Schaltegger, U., and Davies, J. H. (2017). Petrochronology of zircon and baddeleyite in igneous rocks: reconstructing magmatic processes at high temporal resolution. *Rev. Mineral. Geochem.* 83, 297–328. doi: 10.1515/9783110561890-011

Schaltegger, U., Schmitt, A. K., and Horstwood, M. S. A. (2015). U–Th–Pb zircon geochronology by ID-TIMS, SIMS, and laser ablation ICP-MS: recipes, interpretations, and opportunities. *Chem. Geol.* 402, 89–110. doi: 10.1016/j.chemgeo.2015.02.028

Schmitt, A. K. (2009). "Quaternary geochronology by SIMS," in *Mineralogical Association of Canada Short Course 41,* ed M. Fayek (Toronto), 109–131.

Schmitt, A. K., Grove, M., Harrison, T. M., Lovera, O., Hulen, J. B., and Walters, M. (2003). The geysers-cobb mountain magma system California (Part 1): U-Pb zircon ages of volcanic rocks conditions of zircon crystallization and magma residence times. *Geochim. Cosmochim. Acta* 67, 3423–3442. doi: 10.1016/S0016-7037(03)00140-6

Shock, E. L., Helgeson, H. C., and Sverjensky, D. A. (1989). Calculation of the thermodynamic and transport properties of aqueous species at high pressures and temperatures: standard partial molal properties of inorganic neutral species. *Geochim. Cosmochim. Acta* 53, 2157–2183. doi: 10.1016/0016-7037(89)90341-4

Spencer, C. J., Cavosie, A. J., Raub, T. D., Rollinson, H., Jeon, H., Searle, M. P., et al. (2017). Evidence for melting mud in Earth's mantle from extreme oxygen isotope signatures in zircon. *Geology* 45, 975–978. doi: 10.1130/G39402.1

Tang, M., Rudnick, R. L., McDonough, W. F., Bose, M., and Goreva, Y. (2017). Multi-mode Li diffusion in natural zircons: evidence for diffusion in the presence of step-function concentration boundaries. *Earth Planet. Sci. Lett.* 474, 110–119. doi: 10.1016/j.epsl.2017.06.034

Trail, D., Bindeman, I. N., Watson, E. B., and Schmitt, A. K. (2009). Experimental calibration of oxygen isotopic fractionation factors between quartz and zircon. *Geochim. Cosmochim. Acta* 73, 7110–7126. doi: 10.1016/j.gca.2009.08.024

Trail, D., Cherniak, D. J., Watson, E. B., Harrison, T. M., Weiss, B. P., and Szumila, I. (2016). Li zoning in zircon as a potential geospeedometer and peak temperature indicator. *Contrib. Mineral. Petrol.* 171:25. doi: 10.1007/s00410-016-1238-8

Trail, D., Mojzsis, S. J., Harrison, T. M., Schmitt, A. K., Watson, E. B., and Young, E. D. (2007). Constraints on Hadean zircon protoliths from oxygen isotopes Ti thermometry, and rare earth elements. *Geochem. Geophys. Geosyst.* 8:Q06014. doi: 10.1029/2006GC001449

Valley, J. W. (2003). Oxygen isotopes in zircon. *Rev. Mineral. Geochem.* 53 , 343–385. doi: 10.2113/0530343

Valley, J. W., Reinhard, D. A., Cavosie, A. J., Ushikubo, T., Lawrence, D. F., Larson, D. J., et al. (2015). Nano-and micro-geochronology in Hadean and Archean zircons by atom-probe tomography and SIMS: new tools for old minerals. *Am. Mineral.* 100, 1355–1377. doi: 10.2138/am-2015-5134

Watson, E. B., and Cherniak, D. J. (1997). Oxygen diffusion in zircon. *Earth Planet. Sci. Lett.* 148, 527–544. doi: 10.1016/S0012-821X(97)00057-5

Wiedenbeck, M., Hanchar, J. M., Peck, W. H., et al. (2004). Further characterisation of the 91500 Zircon Crystal. *Geostand. Geoanal. Res.* 28, 9–39. doi: 10.1111/j.1751-908X.2004.tb01041.x

Wilde, S. A., Valley, J. W., Peck, W. H., and Graham, C. M. (2001). Evidence from detrital zircons for the existence of continental crust and oceans on the Earth 4.4 Gyr ago. *Nature* 409, 176–178. doi: 10.1038/350 51550

Williams, P., and Baker, J. E. (1981). Implantation and Ion beam mixing in thin film analysis. *Nucl. Instum. Methods* 182, 183, 15–24. doi: 10.1016/0029-554X(81)90667-4

Wotzlaw, J. F., Bindeman, I. N., Stern, R. A., D'Abzac, F. X., and Schaltegger, U. (2015). Rapid heterogeneous assembly of multiple magma reservoirs prior to Yellowstone supereruptions. *Nat. Sci. Rep.* 5:14026. doi: 10.1038/srep 14026